



HAL
open science

Soft-phonon driven hexagonal-orthorhombic phase transition in BaVS 3

Adrien Girard, Michal Stekiel, Wolfgang Morgenroth, Bjoern Winkler, Vita Ilakovac, Alexei Bosak, Helmuth Berger, Tanaka Yoshikazu, Takumi Hasegawa

► **To cite this version:**

Adrien Girard, Michal Stekiel, Wolfgang Morgenroth, Bjoern Winkler, Vita Ilakovac, et al.. Soft-phonon driven hexagonal-orthorhombic phase transition in BaVS 3. *Physical Review B: Condensed Matter and Materials Physics (1998-2015)*, 2019, 99 (14), 10.1103/PhysRevB.99.144104. hal-02375879

HAL Id: hal-02375879

<https://hal.sorbonne-universite.fr/hal-02375879v1>

Submitted on 22 Nov 2019

HAL is a multi-disciplinary open access archive for the deposit and dissemination of scientific research documents, whether they are published or not. The documents may come from teaching and research institutions in France or abroad, or from public or private research centers.

L'archive ouverte pluridisciplinaire **HAL**, est destinée au dépôt et à la diffusion de documents scientifiques de niveau recherche, publiés ou non, émanant des établissements d'enseignement et de recherche français ou étrangers, des laboratoires publics ou privés.

Soft-phonon driven hexagonal-orthorhombic phase transition in BaVS₃

Adrien Girard,* Michal Stekiel, Wolfgang Morgenroth, and Bjoern Winkler
*Institut für Geowissenschaften, Goethe Universität Frankfurt,
Altenhöferallee 1, D-60438 Frankfurt am Main, Germany*

Vita Ilakovac
*Sorbonne Université, CNRS, Laboratoire de Chimie Physique - Matière et Rayonnement, UMR 7614, F-75252 Paris, France and
Université de Cergy-Pontoise, Département de Physique, F-95031 Cergy-Pontoise, France*

Alexei Bosak
ESRF - The European Synchrotron, 71, Avenue des Martyrs, F-38000 Grenoble, France

Helmuth Berger
Institut de Physique de la Matière Complexe, Ecole Polytechnique Fédérale de Lausanne, CH-1015 Lausanne, Switzerland

Tanaka Yoshikazu
RIKEN Spring-8 Center, Sayo, Hyogo 679-5148, Japan

Takumi Hasegawa
*Graduate School of Integrated Arts and Sciences,
Hiroshima University, Higashi-Hiroshima, Hiroshima 739-8521, Japan.*
(Dated: November 12, 2019)

The lattice dynamics of low-dimensional BaVS₃ is reported across the hexagonal-orthorhombic phase transition occurring at $T_S = 250$ K using a combination of Thermal Diffuse Scattering of X-rays, Inelastic X-ray Scattering and DFT calculations. We observed the occurrence of strongly temperature-dependent diffuse scattering upon approaching the transition, centered at the Γ points associated with weak Bragg reflections with odd L . Inelastic scattering experiment related this observation to the condensation of a low-lying overdamped optical phonon at the Brillouin zone center, evidenced by significant variations of quasi-elastic scattering. These results unravel the dynamical origin of the zigzag distortion of the V chains at T_S , which is probably a prerequisite of the Peierls anomaly driving the metal-insulator transition at $T_{MI} = 70$ K.

I. INTRODUCTION

BaVS₃ is a low-dimensional strongly correlated electronic system undergoing a remarkable succession of three phase transitions whose origin is still under discussion. Its room temperature (RT) structure¹ consists of a hexagonal packing of quasi 1D-chains of face-sharing VS₆ octahedra directed along the c axis. The structural anisotropy suggests properties of a linear chain compound, but with a surprisingly low conductivity anisotropy ratio σ_c/σ_a of only 3² while it can reach 10⁵ in 1D conductors³. A zigzag deformation of the V chains at $T_S = 250$ K reduces the crystal symmetry from hexagonal to orthorhombic. This displacive second order phase transition does not introduce any significant change in the resistivity and the paramagnetic properties^{1,4}. The electronic properties (resistivity, thermoelectric power) change below the resistivity minimum (130 K)^{1,5} and an extra feature shows up in the pre-edge of the V L-edge linear dichroism⁶. On further cooling, the system undergoes a metal-to-insulator transition (MI) at $T_{MI} = 70$ K, accompanied by a doubling of the unit cell in the c direction⁷. The driving force of the MI transition is the Peierls instability resulting in formation of charge density waves (CDW) along the V chains, shown by pre-

transitional diffuse streaks at the wave vector $2k_F = 0.5 c^*$. They appear already at 170 K, but the CDW transition occurs only at 70 K. Spin degrees of freedom are affected at T_{MI} ², but an incommensurate antiferromagnetic order establishes only below $T_N = 30$ K⁹⁻¹².

Physical properties of BaVS₃ point to a subtle interaction between itinerant and localized electrons. The critical CDW wave vector $2k_F = 0.5 c^*$ indicates that only one of the two d electrons per unit cell is delocalized at high temperature and quenches at T_{MI} ⁸, while an effective local-moment corresponding to 1/2 spin per two V sites is estimated from the magnetic susceptibility². LDA calculations reveal effectively an interplay between two different types of active electrons at the Fermi level: two narrow E_g bands, and one dispersive, with mainly A_{1g} character, extending along the c^* direction¹³⁻¹⁸.

The intriguing low-temperature physics of BaVS₃ rely heavily on the electronic changes occurring at T_S through the orthorhombic distortion, which stabilizes the structure hosting the MI transition. However, after 40 years of research on this material, the driving force for the orthorhombic transition still remains controversial, which motivated this study. In this paper, we present an investigation of the lattice dynamics of BaVS₃ across the transition at T_S . First we used temperature-dependent

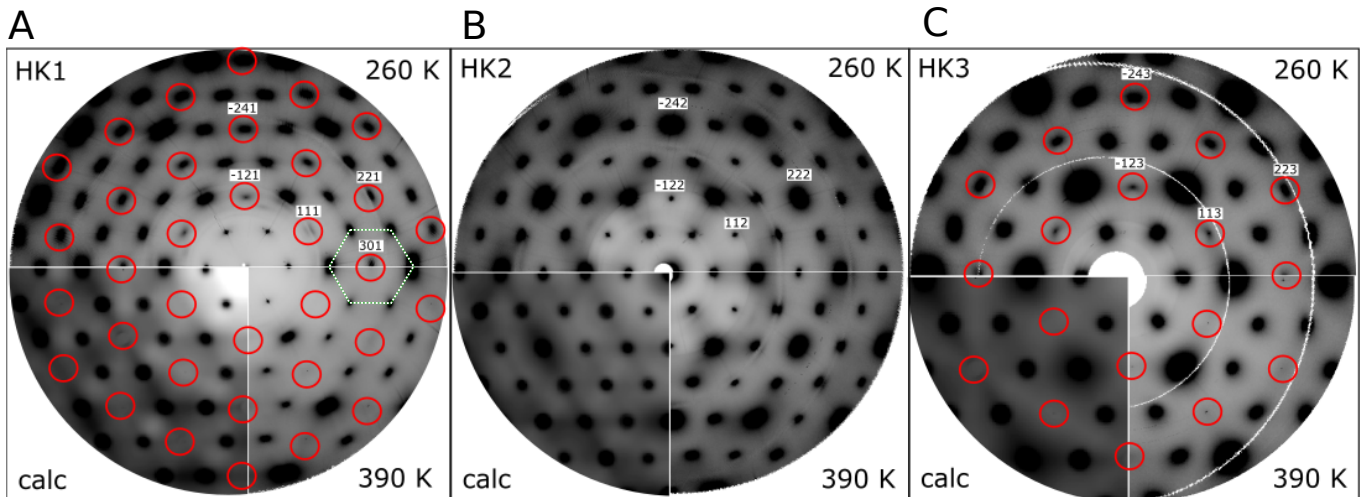


FIG. 1. A, B, C: Reciprocal space maps of BaVS_3 in HK1, HK2 and HK3 planes respectively, recorded at 260 K (upper panels) and 390 K (lower right panels), compared to the calculations (lower left panels). Red circles denote the reciprocal space nodes where the soft mode freezing produces changes of TDS intensity. The white hexagon is centered on the 301 reflection that was used for the phonon study. The maps are indexed in hexagonal setting, which is used throughout this study.

Thermal Diffuse Scattering (TDS) to pinpoint the occurrence of a phonon anomaly at the orthorhombic transition, which was further investigated in more details with Inelastic X-ray Scattering (IXS). The IXS data unambiguously revealed the condensation of a low-energy optical phonon at T_S . The experimental results are confronted with DFT calculations, which pictured the structural instability in the hexagonal phase at the Brillouin zone center. Finally the driving force for the orthorhombic distortion is discussed.

II. EXPERIMENTAL DETAILS

Single crystals of BaVS_3 were grown by the tellurium flux method¹⁹. The crystal was mounted on a glass fiber and fixed with an epoxy glue. Crystal quality is shown through IXS alignment scans in the annex section. The stoichiometry was analyzed by wavelength dispersive spectroscopy, which showed the presence of a tiny amount of Al (0.54%) and a surface layer of \sim few hundreds nm contaminated by Cu with content $(5.2 \pm 3.2)\%$, originating from the resulfurization process which was performed by annealing in the H_2S atmosphere, while a part of the tubes for the gas was made of copper. The crystal was cut and polished in the shape of a needle oriented along the $[001]$ axis, with a lateral dimension of about $100 \mu\text{m}$, in order to maximize the IXS signal. X-ray thermal diffuse experiments were conducted first with the diffractometer built as a side station at the ID28 beamline of the European Synchrotron Radiation Facility (ESRF), with a monochromatic beam of 17.8 keV photons. The TDS maps were recorded at ID28 side station²⁰ with a Pilatus $3 \times 1\text{M}$ detector at temperatures between 150 K and 390 K controlled to within ± 5

K with an Oxford Cryostream 700 plus cooling system. The IXS experiments were conducted at the ID28 beamline of the ESRF, with the high resolution spectrometer operated at an energy of 17.8 keV. With our setup, the energy resolution was 3 meV. The temperature was controlled with the same cryostream cooling system as for the TDS experiment.

III. COMPUTATIONAL DETAILS

First-principles calculations were carried out within the framework of density-functional theory (DFT)²¹ and the pseudopotential method using the CASTEP²² simulation package. "On-the-fly ultrasoft" norm-conserving pseudopotentials from the CASTEP data base were employed in conjunction with plane waves up to a kinetic energy cutoff of 420 eV. A Monkhorst-Pack grid was used for Brillouin-zone integrations with a distance of $< 0.028 \text{ \AA}^{-1}$ between grid points. Convergence criteria included an energy change of $< 5 \times 10^{-6} \text{ eV/atom}$ for scf-cycles, a maximal force of $< 0.006 \text{ eV/\AA}$, and a maximal component of the stress tensor $< 0.01 \text{ GPa}$. The phonons were computed by finite difference calculations with a cut-off for interaction $> 8.1 \text{ \AA}$.

IV. RESULTS

The conventional room temperature (RT) BaVS_3 structure is hexagonal, with the space group $P6_3/mmc^1$ and lattice parameters $a_H = b_H = 6.719 \text{ \AA}$, $c_H = 5.619 \text{ \AA}$ ²³. Below T_S , its symmetry is reduced to the orthorhombic space group $Cmc2_1^4$, with lattice parameters $a_O = 6.75 \text{ \AA}$, $b_O = 11.48 \text{ \AA}$, $c_O = 5.6 \text{ \AA}$ ^{23,24}. Our calcu-

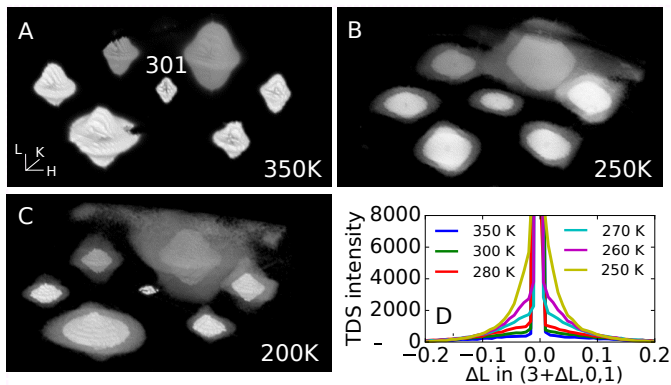


FIG. 2. A, B, C: 3D reciprocal space reconstructions of the TDS signal indicated by a white hexagon in the Fig.1A, measured at 350 K, 250 K, 200 K respectively. It shows how the spatial distribution of the TDS intensity changes upon crossing the transition at T_S . The (301) Brillouin zone, where the soft mode has highest intensity, was selected for the IXS study. D: 1D TDS profile along the direction $(3+\Delta L,0,1)$.

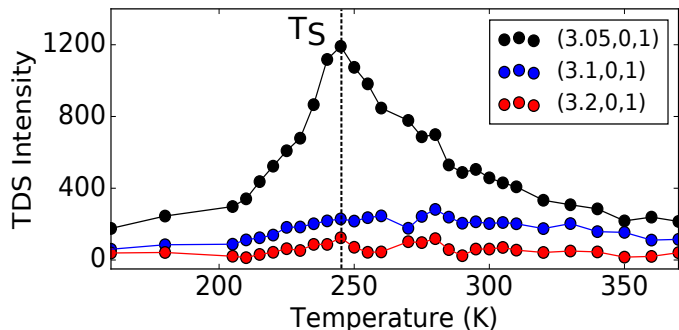


FIG. 3. Temperature evolution of the TDS intensity measured at $(3.05,0,1)$, $(3.1,0,1)$ $(3.2,0,1)$.

lated lattice parameters agree with the experimental ones within 2% ($a_H^{\text{DFT}} = b_H^{\text{DFT}} = 6.791 \text{ \AA}$, $c_H^{\text{DFT}} = 5.561 \text{ \AA}$, and $a_O^{\text{DFT}} = 6.786 \text{ \AA}$, $b_O^{\text{DFT}} = 11.749 \text{ \AA}$, $c_O^{\text{DFT}} = 5.577 \text{ \AA}$). We first carried out a TDS experiment across the transition at T_S to map out in the reciprocal space the weak features related to inelastic scattering of the x-rays by the phonons.

The experimental reconstructed reciprocal space maps recorded in the hexagonal phase above T_S at $T = 390 \text{ K}$ and close to T_S at $T = 260 \text{ K}$ are shown in Fig. 1.A, B, C for the planes HK1, HK2 and HK3 respectively. The experimental maps are compared to the calculated ones (lower left panels), where an overall good agreement is observed with the high temperature data. However, additional diffuse scattering features are observed in HK1 and HK3 planes upon approaching T_S , as displayed in the maps with odd L acquired at 260 K (lower right panels). Just above the transition, a strong TDS signal is detected close to the Γ points of the Brillouin zones with odd L (red circles).

The evolution of the TDS intensity distribution around

a set of selected Bragg reflections centered around (301) can be better visualized with 3D reconstructions in Fig. 2 upon cooling from the hexagonal down to the orthorhombic phase. The seven reflections displayed in 3D belong to the HK1 plane and are indicated with a white hexagon in Fig. 1.A. At high temperature, the constant intensity contours are well defined and the anisotropic distribution results from the elastic anisotropy of the crystal. Close to the transition at about $T = 250 \text{ K}$, the intensity distribution becomes more diffuse, and shrinks along c^* while it widens in the (a^*b^*) plane resulting in a disc-shaped pattern. The effect is most evident around the weak (301) reflection where the contribution of the acoustic phonons is weaker, pointing at the softening of an optical phonon in the hexagonal plane. In order to better visualize these intensity variations, the corresponding 1D intensity profiles across the (301) reflection is shown for different temperatures in Fig. 2.D along $(3+\Delta L,0,1)$ direction. It shows the gradual appearance of the TDS intensity upon approaching the transition, which peaks at T_S . The TDS intensity at $\Delta L = 0.05$, $\Delta L = 0.1$ and $\Delta L = 0.2$ is reported as a function of the temperature in Fig. 3. For $T > 330 \text{ K}$ the Bragg peak is sharply localized and the diffuse intensity is very weak. As the temperature is decreased the diffuse intensity increases and reaches a maximum at $T=245 \text{ K}$. The effect is most pronounced in the vicinity of Γ : it is very strong at $\Delta L = 0.05$, weak at $\Delta L = 0.1$ and disappears for $\Delta L > 0.15$. The TDS intensity then rapidly decreases after the orthorhombic phase transition, for $T < T_S$.

In a TDS measurement, there is no energy analysis and it is therefore not straightforward (i) to disentangle the static and dynamic contributions to the observed signal and (ii) in case of inelastic scattering by a soft mode, to identify which phonon branch softens. To get further insights about the dynamical origin of the observed diffuse features, we have performed a temperature dependent IXS experiment, which provides energy and momentum resolved measurements of the phonon dispersion. In the following we focus on the (301) reflection which showed the most pronounced effect. The phonon dispersion measured at 400 K along $(3+\Delta L,0,1)$ for $0.1 \leq \Delta L \leq 0.5$ is shown in Fig. 4.A for energy transfers up to 20 meV, and the extracted energies are reported in Fig. 4.B. Within this energy range the IXS spectra is composed of a weak elastic peak and three optical phonons in the Stokes and anti-Stokes part of the IXS spectra whose intensities are related by the detailed balance principle. Excitations were fitted using a Damped Harmonic Oscillator (DHO) model and a central line convoluted with the experimental resolution function.

In order to identify the soft-mode, we have followed the temperature dependence of the low-energy optical phonons. The evolution of the IXS spectra with temperature is shown in Fig. 5.A and B between 500 K and 180 K. The phonon softening occurs at Γ , which is inaccessible to IXS measurements because the inelastic signal is obscured by the strong elastic scattering of the

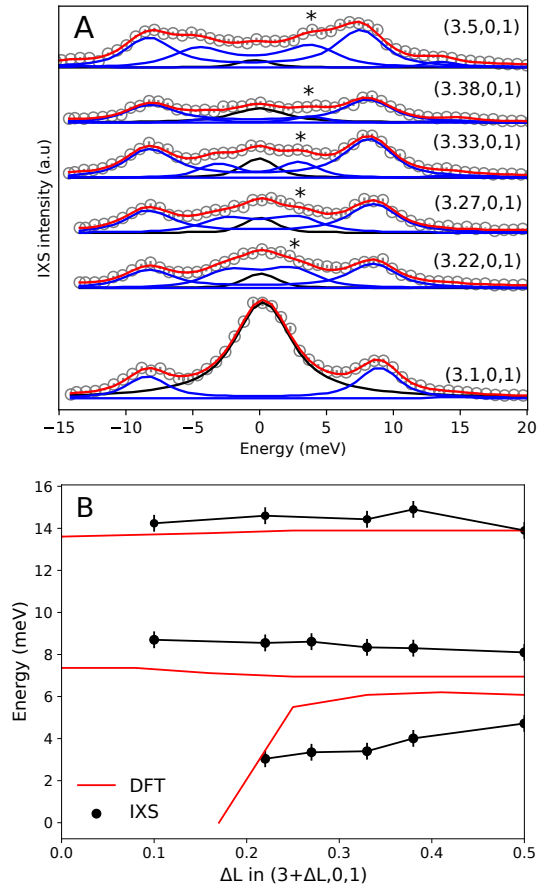


FIG. 4. A: Fit of the IXS spectra measured in the vicinity of the (301) reflection at 400 K, showing the dispersion of the soft phonon (marked with an *) along the direction $(3+\Delta L,0,1)$. Blue lines: DHO excitations, black: central peak, red: total model. B: Comparison between experimental phonon energies extracted from IXS and calculated energies from DFT.

Bragg reflection. Therefore we have selected a region of reciprocal space as a compromise between the geometrical constraints of the measurement, the elastic intensity at zero energy transfer and the phonon energy close to Γ . The best compromise was obtained for $\Delta L = 0.1$ in $(3+\Delta L,0,1)$, where the softening is much less pronounced than for $\Delta L = 0.05$ (as inferred from the TDS intensity in Fig. 2), but still sufficient to be observable in the IXS measurement. At 500 K, the central peak is weak in intensity and the contribution of the lowest energy phonon at ~ 3 meV can hardly be distinguished, as its energy lies at the limit of the resolution of our experiment. Upon decreasing the temperature the phonon peak merges with the elastic scattering signal into a broad central line due to the phonon softening. Therefore, we followed the intrinsic width of the central line with temperature rather than the phonon energy, see Fig. 5.C. It decreases continuously from 6.5 meV down to a minimum value 2.2 meV at T_S , which is not resolution limited (a DHO excitation with 0 meV intrinsic width corresponds to the resolution

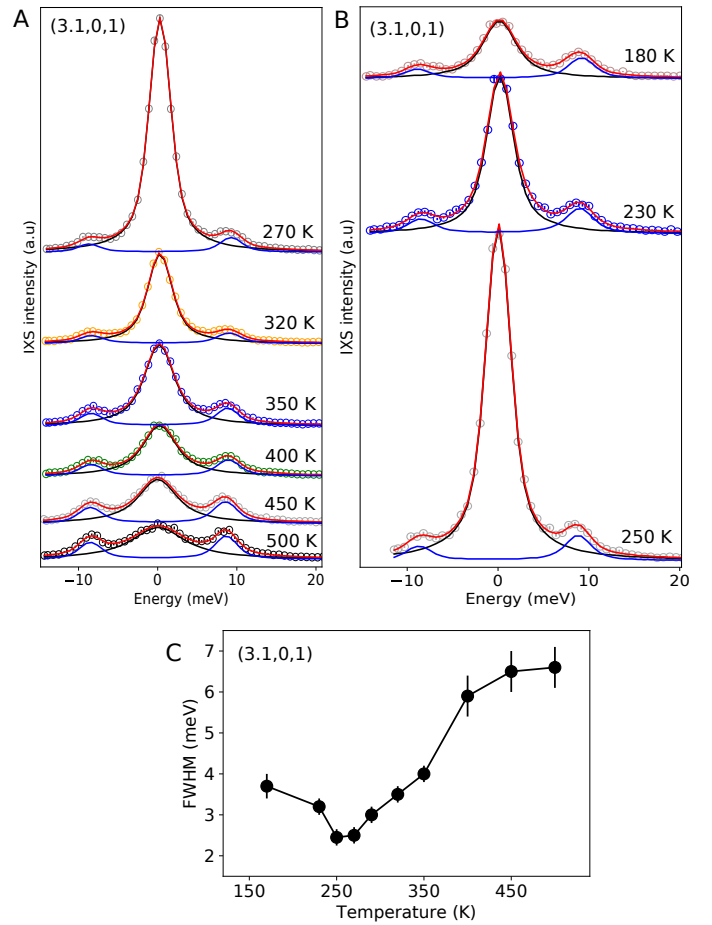


FIG. 5. Evolution of the (3.1,0,1) IXS spectra with temperature, showing the soft mode condensation when approaching T_S from above (A) and cooling below T_S (B). C: Temperature evolution of the central line intrinsic width. Black: central peak, blue: phonon excitation, red: total model (error bars are from the fitting procedure).

limit of the experiment, *i.e.* 3 meV peak width). Upon further cooling below T_S , the intrinsic width increases back. This can be explained by the soft-phonon hardening after the settling of the orthorhombic transition, as observed in other compounds^{25,26}. Some electron-phonon coupling mechanism could be involved, the study of which lies outside the scope of this work.

Our experimental data were compared to the DFT results. The calculations of the phonon dispersion in the hexagonal structure show a phonon instability at the Γ point of the hexagonal structure, as evidenced by imaginary phonon frequencies in a narrow q -range centered on the Γ -point (Fig. 6). The instability is not present in the orthorhombic structure, where the unstable phonon mode recovers a real and positive energy. Interestingly we found that the transition is accompanied by a collapse of a set of high energy optical branches with $E > 50$ meV in the hexagonal phase. The low energy range < 20 meV of the calculated dispersion is displayed and compared to

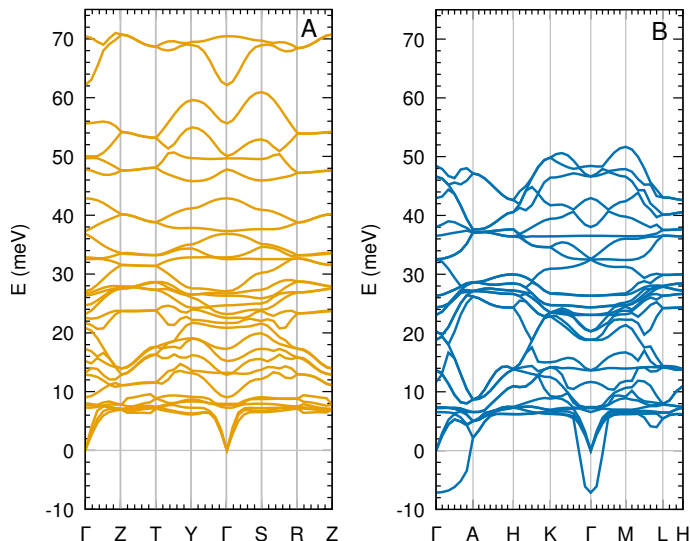


FIG. 6. Calculated phonon dispersion of BaVS₃ in A) the orthorhombic phase and B) the hexagonal phase. The unstable optical phonon at Γ is characterized by negative frequency in the hexagonal phase.

the IXS results in Fig 4.B. The lowest energy ~ 5 meV optical phonon shows an anomaly for $\Delta L < 0.2$. This value matches with the ΔL value at which we observed the collapse of the phonon mode into the elastic line (Fig 4.A and B). The distortion vector of the structural transition, showing how atoms are displaced through the transition (Fig. 7.A), is to be compared with the soft mode eigenvector at the Γ point. The phonon displacement pattern involves mainly a torsion of the sulfur (S) octahedra, where the S of neighbouring chains vibrate in phase (Fig. 7.B). The V atoms show smaller displacement and cannot be visualized in the same scale. Their displacements is displayed in Fig. 7.C for a better visualization. It consists of a twisting of the vanadium (V) atoms perpendicular to the chains, similar to the distortion of the V chains occurring at the transition, where the condensation of both S and V displacements leads to the strongly distorted VS₆ octahedra in the low temperature phase.

V. DISCUSSION

The transition at T_S was previously theoretically studied by Lechermann *et al*^{16–18}. Above T_S , the Fermi level is shared by delocalized A_{1g} states and two degenerate E_g states. Below T_S , there is a splitting of E_g states, one stabilized (named E_{g1}) and more hybridized with A_{1g} states, while the other (named E_{g2}) pushed to higher energy²⁷. The reinforced A_{1g} - E_{g1} hybridization below T_S is not obviously at the origin of the hexagonal-orthorhombic transition, but can be seen as its order parameter.

Other works speculated that the transition at T_S may

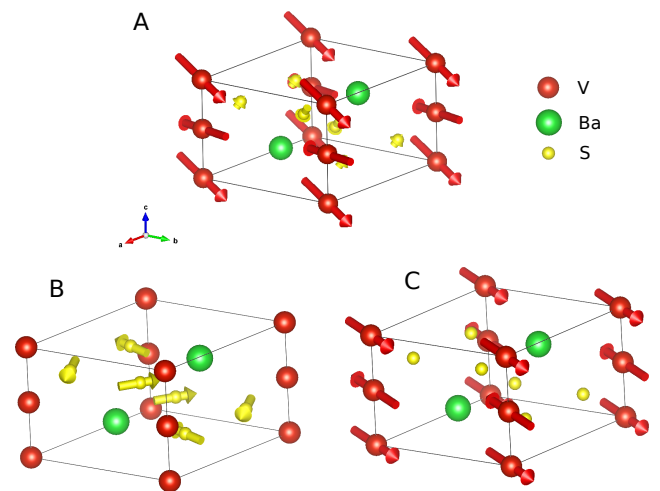


FIG. 7. A. Distortion vector of the hexagonal to orthorhombic transition. B. Visualization of the soft mode eigenvector at Γ in the hexagonal setting. C. Enlarged view of the V atoms displacement where the much larger S displacements have been omitted for clarity.

be soft phonon driven. Ultrasonic measurements across T_S showed a decrease of 11% and 17% of the longitudinal and transverse velocities respectively at the transition and high attenuation²⁸. The results were qualitatively interpreted in terms of interaction between a soft mode phonon and elastic distortion produced at the transition. However, Raman data in both hexagonal and orthorhombic phases showed no observable influence of the distortion on the lattice dynamics of BaVS₃²⁹. A more detailed Raman study of the phonons revealed a number of anomalous changes in frequency and linewidth upon cooling from T_S to T_X but the soft mode responsible for the orthorhombic transition at T_S could not be observed³⁰. In the light of the present results, it becomes clear that the soft mode energy was too low to be observed with a standard Raman equipment.

Our observations for BaVS₃ point to two main conclusions. First, we provide plausible evidence that the hexagonal-orthorhombic transition at T_S is driven by an overdamped soft optical phonon. One argument is that the calculated displacement pattern of the unstable phonon matches the well established distortion of the vanadium chains occurring at the transition. Then, the observed TDS intensity follows the relationship $I_{TDS} \propto |F(h, k, l)|^2 q^{-2}$ which is expected for diffuse scattering arising from low energy phonons, see Fig. 8 where $q = \Delta L$. On the other hand, the hypothesis of order-disorder dynamics and cluster nucleation would produce a dependence $I \propto |F(h, k, l)|^2$, with a resolution limited central peak. At 350K, far from the transition, the soft phonon has relatively high energy, and the TDS signal is not observed. The Bragg peak is sharply localized in reciprocal space, as shown in Fig. 2.D. This strong temperature dependence of the TDS tail close to the transition

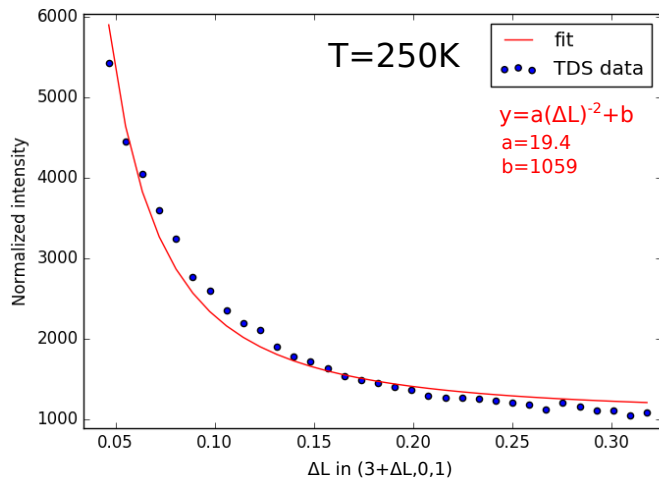


FIG. 8. L dependence of the TDS intensity measured in the direction ΔL in $(3+\Delta L,0,1)$ at $T = 250$ K, showing the ΔL^{-2} power law originating from the inelastic phonon scattering. The intensity is normalized to the incoming beam intensity.

is a clear indication of phonon softening. Additionally, the unstable phonon has substantial TDS intensity at the Γ point of the Brillouin zones. As unstable modes have imaginary frequencies in the calculations, the imaginary part of the dispersion was cut in order to calculate the TDS intensity in the reciprocal space maps shown in Fig. 1, which require positive real phonon energies. This removal procedure results in greyed-out areas in Fig. 1.A and C corresponding to the reciprocal space part where the unstable mode had imaginary frequencies. These greyed-out areas correspond to the areas where the strong TDS effect is observed experimentally, which furthermore confirms that the observed effect are of inelastic nature. The soft mode freezing can occur together with some order-disorder dynamics, where clusters of the low temperature phase nucleate and grow in the high temperature structure upon cooling, as these two processes are not mutually exclusive and can act together. However the arguments presented here and the fact that the effects start at relatively high temperature (340 K for the TDS) clearly point at a dominant contribution of the displacive dynamics, where the orthorhombic transition is driven by the condensation of the unstable soft phonon.

Second, the S atoms also play an important role in the lattice instability, as the amplitude of the S displacement in the soft mode is about two orders of magnitude larger than that of the V atoms. This emphasizes the importance of the S atoms in the properties of BaVS_3 throughout the whole set of low temperature phase transitions, which has been already pointed out in numerous earlier studies. It was observed that in sulfur deficient $\text{BaVS}_{3-\delta}$ with $\delta = 0.12$, the transition at T_S is lowered down to 150 K³¹. Sulfur deficiency also impact the magnetism, with a ferromagnetic order that sets in below 16 K ($\delta \leq 0.2$), instead of antiferromagnetic order^{31,32}. For

non stoichiometric $\text{BaVS}_{3-\delta}$, the Peierls distortion is replaced by an incommensurate modulation due to a charge ordering associated with the localized E_g electrons^{33,34}. Finally, linear dichroism experiments have pointed out the progressive depletion of S $3p_z - V 3d_z^2$ hybridization associated with the zig-zag deformation of VS_6 octahedra chains³⁵.

Finally, let us briefly discuss the relation of the soft phonon and the electronic structure of BaVS_3 . First, an estimation of the dimensionless electron-phonon coupling of a particular mode can be given on the basis of IXS data by the expression taken from A. Shukla *et al*^{36,37}:

$$\lambda = \frac{\gamma}{2\pi N(0)(\hbar\omega)^2} \quad (1)$$

where γ is the FWHM linewidth, $N(0)$ the density of states at the Fermi level and $\hbar\omega$ the frequency of the mode. The expression supposes that the linewidth broadening due to anharmonic effects is negligible.

For the mode which softens at the hexagonal to orthorhombic transition, we take from fit of the data at $T = 500$ K: the linewidth $\gamma = (2 \pm 0,5)$ meV, the vibrational energy of the mode $\hbar\omega = (3,8 \pm 0,5)$ meV and the total density of the states at the Fermi level per formula unit (BaVS_3) $N(0) = (10 \pm 2)$ eV⁻¹. The first two values are from our work, while $N(0)$ is taken from the Fig.2 in Ref.¹⁸. These values give us an estimation of λ of 2,2 with a relative error of 70%. The value of λ is comparable to this of a vibrational mode in MgB_2 (2.5-3.6³⁶), which is a phonon-mediated superconductor. The mode width and energy could be obtained reliably only at high temperature (500 K), where it is most separated from the elastic line and the phonon is not overdamped. These conditions are far from ideal low temperature conditions and harmonic approximation. Given that anharmonic effects are also neglected, this value rather presents a rough estimation of the highest limit of λ .

Second, the soft phonon appears at gamma point, where the Fermi surface shows a substantial E_{g2} electron pocket in the orthorhombic phase, and no states in the hexagonal phase (Fig. 5 Ref.¹⁸). Thus we can tentatively say that the soft phonon is mostly coupled to the E_{g2} states, which are, relatively to the E_{g1} states, pushed to higher energy in the orthorhombic phase.

We hope that our study will motivate more theoretical considerations, including coupling of electrons and phonons, in order to discuss more deeply our scenario. A theoretical study of the optical conductivity including electrons and phonons was performed in the mid-infrared range (155-413 meV) for quarter-filled CDW systems, like BaVS_3 ³⁸. But here the photon energy is too high compared to the energy of the soft phonon which we observed (2 meV).

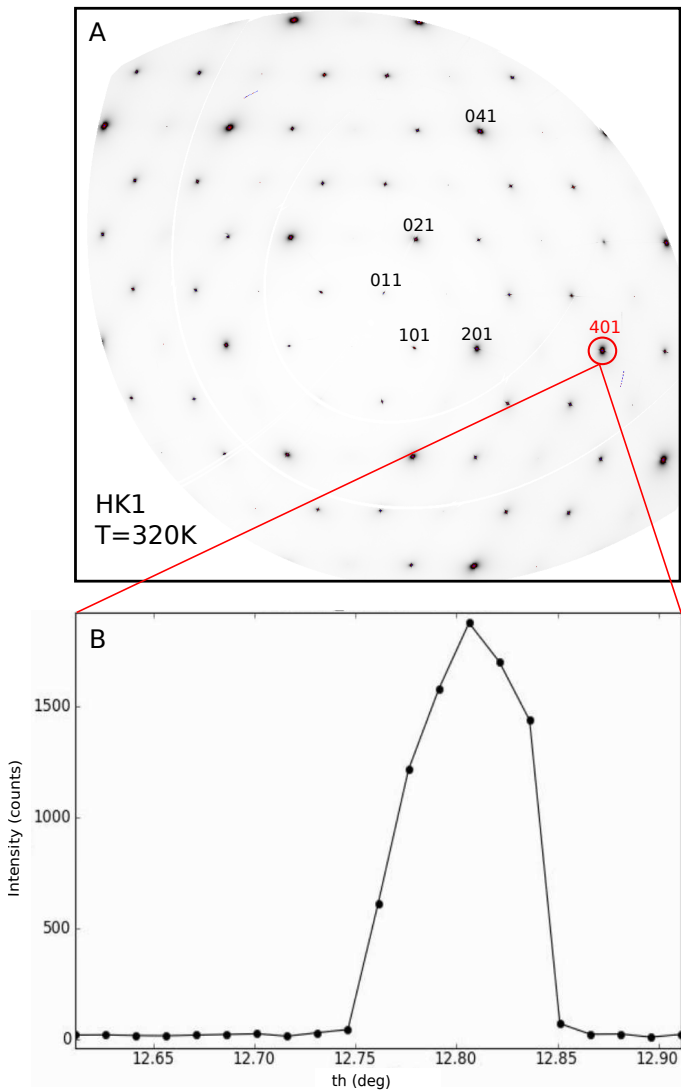


FIG. 9. A. Reconstruction of the HK1 plane using high dynamic range color scale. B. Theta scan around the 401 Bragg peak using the high resolution arm of the IXS spectrometer.

VI. CONCLUSION

In summary, we have studied the hexagonal-orthorhombic transition occurring in BaVS_3 at $T_S = 250$ K using a combination of TDS, IXS and DFT calculations. The softening of a low energy overdamped optical phonon at the Brillouin zone center was evidenced by strong variations of the TDS intensity distribution around the weak Bragg reflections with odd L .

The phonon condensation was captured on both sides of the transition using energy and momentum resolved IXS measurements. The hypothesis of a soft-phonon driven phase transition was confirmed by our DFT calculations, which evidenced an imaginary frequency of the soft mode at the Γ point. In addition to unraveling the dynamical origin of the transition at T_S , these results point to the importance of the S for the properties of BaVS_3 , as the orthorhombic distortion sets the electronic configuration favorable for the Peierls instability driving the metal-insulator transition at lower temperature. Finally, this work demonstrates the advantages of combining TDS + IXS + DFT studies for the investigation of phase transitions in crystalline matter.

VII. ANNEXES

In order to assess the quality of the BaVS_3 crystal used in our experiment, it is useful to look at the sharpness of the Bragg reflections. The reciprocal space map reconstructions presented in Fig.9.A give an overview of the Bragg spots in the HK1 plane, where the position of each Bragg is indicated by saturated pixels. Here, unlike in Fig 1, where a grey colorscale was used, a high dynamic range color scale allows to distinguish the intensity variations and to dissociate the position of the Bragg reflections and the strong diffuse scattering. The sharp localization of the observed reflections attests the good quality of the crystal. This is further confirmed in Fig 9.B by the theta scan of the sample using the high resolution arm of the IXS spectrometer. Here the scan was performed around the 401 reflection used to obtain the orientation matrix of the crystal. The measured peak width of $\sim 0.1^\circ$ is a standard value for good quality crystals.

VIII. ACKNOWLEDGEMENTS

This study was supported by BMBF projects 05K13RF1 and 05K13RF2 and a joint DFG-ANR project WI1232/41-1. We thank Denis Gambetti for technical support in the operation of ID28 beamline of the ESRF. We thank Michel Fialin, CAMPARIS, IPGP, Sorbonne Université, for the Wavelength Dispersive Spectroscopy (WDS) measurements. Critical reading of the manuscript by Jean-Paul Pouget is gratefully acknowledged.

* Corresponding author: adrien.girard@sorbonne-universite.fr

¹ R. A. Gardner, M. Vlasse, and A. Wold, Acta Crystallographica Section B **25**, 781 (1969).

² G. Mihaly, I. Kezsmarki, F. Zamborszky, M. Miljak, K. Penc, P. Fazekas, H. Berger, and L. Forro, Phys. Rev. B **61**, 4 (1999), arXiv:9911122 [cond-mat].

³ H. Zeller and A. Beck, Journal of Physics and Chemistry

- of Solids **35**, 77 (1974).
- ⁴ F. Sayetat, M. Ghedira, M. Marezio, and J. Chenavas, *Journal of Physics C: Solid State Physics* **15**, 1627 (1982).
 - ⁵ N. Barisic, , Ph.D. thesis, EPFL (2004).
 - ⁶ V. Ilakovac, N. B. Brookes, J. C. Cezar, P. Thakur, V. Bisogni, C. Dallera, G. Ghiringhelli, L. Braicovich, S. Bernu, H. Berger, L. Forró, A. Akrap, and C. F. Hague, *Journal of Physics, Condensed Matter* **24**, 045503 (2012).
 - ⁷ T. Inami, K. Ohwada, H. Kimura, M. Watanabe, Y. Noda, H. Nakamura, T. Yamasaki, M. Shiga, N. Ikeda, and Y. Murakami, *Phys. Rev. B* **66**, 73108 (2002).
 - ⁸ S. Fagot, P. Foury-Leylekian, S. Ravy, J. Pouget, and H. Berger, *Physical Review Letters* **90**, 196401 (2003).
 - ⁹ H. Nakamura, T. Yamasaki, S. Giri, H. Imai, M. Shiga, K. Kojima, M. Nishi, K. Kakurai, and N. Metoki, *Journal of the Physical Society of Japan* **69**, 2763 (2000).
 - ¹⁰ P. Leininger, V. Ilakovac, Y. Joly, E. Schierle, E. Weschke, O. Bunau, H. Berger, J.-P. Pouget, and P. Foury-Leylekian, *Phys. Rev. Lett.* **106**, 167203 (2011).
 - ¹¹ R. A. de Souza, U. Staub, V. Scagnoli, M. Garganourakis, Y. Bodenthin, and H. Berger, *Phys. Rev. B* **84**, 014409 (2011).
 - ¹² P. Foury-Leylekian, P. Leininger, V. Ilakovac, Y. Joly, S. Bernu, S. Fagot, and J. Pouget, *Physica B, Condensed Matter* **407**(11), 1692 (2012).
 - ¹³ M. Nakamura, A. Sekiyama, H. Namatame, A. Fujimori, H. Yoshihara, T. Ohtani, A. Misu, and M. Takano, *Phys. Rev. B* **49**, 16191 (1994).
 - ¹⁴ L. Mattheiss, *Solid State Communications* **93**, 791 (1995).
 - ¹⁵ M.-H. Whangbo, H.-J. Koo, D. Dai, and A. Villesuzanne, *Journal of Solid State Chemistry* **165**, 345 (2002).
 - ¹⁶ F. Lechermann, S. Biermann, and A. Georges, *Phys. Rev. Lett.* **94**, 166402 (2005).
 - ¹⁷ F. Lechermann, A. Georges, A. Poteryaev, S. Biermann, M. Posternak, A. Yamasaki, and O. K. Andersen, *Phys. Rev. B* **74**, 125120 (2006).
 - ¹⁸ F. Lechermann, S. Biermann, and A. Georges, *Phys. Rev. B* **76**, 085101 (2007).
 - ¹⁹ H. Kuriyaki, H. Berger, S. Nishioka, H. Kawakami, K. Hirakawa, and F. Lévy, *Synthetic Metals* **71**, 2049 (1995), proceedings of the International Conference on Science and Technology of Synthetic Metals (ICSM '94).
 - ²⁰ A. Girard, T. Nguyen-Thanh, S. M. Souliou, M. Stekiel, W. Morgenroth, L. Paolasini, A. Minelli, D. Gambetti, B. Winkler, and A. Bosak, *Journal of Synchrotron Radiation* **26**, 272 (2019).
 - ²¹ P. Hohenberg and W. Kohn, *Phys. Rev.* **136**, B864 (1964).
 - ²² S. J. Clark, M. D. Segall, C. J. Pickard, P. J. Hasnip, P. M. J. Probert, K. Refson, and M. C. Payne, *Z. Kristallogr.* **220**, 567 (2005).
 - ²³ M. Ghedira, M. Anne, J. Chenavas, M. Marezio, and F. Sayetat, *Journal of Physics C: Solid State Physics* **19**, 6489 (1986).
 - ²⁴ S. Fagot, P. Foury-Leylekian, S. Ravy, J. Pouget, M. Anne, G. Popov, M. Lobanov, and M. Greenblatt, *Solid State Sciences* **7**, 718 (2005), a tribute to Erwin Felix Bertaut.
 - ²⁵ S. M. Souliou, Y. Li, X. Du, M. Le Tacon, and A. Bosak, *Phys. Rev. B* **94**, 184309 (2016).
 - ²⁶ M. Maschek, D. A. Zocco, S. Rosenkranz, R. Heid, A. H. Said, A. Alatas, P. Walmsley, I. R. Fisher, and F. Weber, *Phys. Rev. B* **98**, 094304 (2018).
 - ²⁷ The numbers 1/2 in the E_{g1}/E_{g2} notation are introduced to distinguish the two electronic states which split below T_S , in order to keep the hexagonal phase notation A_{1g}/E_g in the whole temperature range.
 - ²⁸ E. K. G. Masahiko S., Mitsue K., Mikio T., Norihiko N., *Japanese Journal of Applied Physics* **18**, 717 (1979).
 - ²⁹ Z. V. Popović, G. Mihály, I. Kézsmárki, H. Berger, L. Forró, and V. V. Moshchalkov, *Physical Review B* **65**, 132301 (2002).
 - ³⁰ K. Choi, D. Wulferding, H. Berger, and P. Lemmens, *Physical Review B* **80**, 245108 (2009).
 - ³¹ O. Massenet, R. Buder, J. Since, C. Schlenker, J. Mercier, J. Kelber, and D. Stucky, *Materials Research Bulletin* **13**, 187 (1978).
 - ³² T. Yamasaki, H. Nakamura, and M. Shiga, *Journal of the Physical Society of Japan* **69**, 3068 (2000), <https://doi.org/10.1143/JPSJ.69.3068>.
 - ³³ S. Bernu, P. Foury-Leylekian, J. Pouget, A. Akrap, H. Berger, L. Forro, G. Popov, and M. Greenblatt, *Physica B: Condensed Matter* **403**, 1625 (2008).
 - ³⁴ S. Bernu, P. Foury-Leylekian, P. Fertey, F. Licci, A. Gauzzi, A. Akrap, H. Berger, L. Forró, and J.-P. Pouget, *EPL (Europhysics Letters)* **89**, 27006 (2010).
 - ³⁵ V. Ilakovac, S. Boulafta, Y. Joly, A. M. Flank, P. Lagarde, M. Žitnik, M. Fialin, H. Berger, and L. Forró, *Physica B: Condensed Matter* **460**, 191 (2015).
 - ³⁶ A. Shukla, M. Calandra, M. d'Astuto, M. Lazzeri, F. Mauri, C. Bellin, M. Krisch, J. Karpinski, S. M. Kazakov, J. Jun, D. Daghero, and K. Parlinski, *Phys. Rev. Lett.* **90**, 095506 (2003).
 - ³⁷ P. B. Allen, *Phys. Rev. B* **6**, 2577 (1972).
 - ³⁸ Kupci'c, I., *Eur. Phys. J. B* **62**, 27 (2008).